Alfvén Speed Transition Zone in the Solar Corona

David B. Wexler[1] , Michael L. Stevens[2] , Anthony W. Case[2] , and Paul Song[1]
[1] Space Science Laboratory, University of Massachusetts Lowell, Lowell, MA, USA; David_Wexler@uml.edu
[2] Smithsonian Astrophysical Observatory, Cambridge, MA, USA

Abstract

The Alfvén radius, r_A, at which solar wind radial outflow speed exceeds the Alfvén wave speed, is an important parameter in understanding solar wind evolution in the extended corona. The mean solar wind angular momentum scales with r_A^2 in the axisymmetric steady-state approximation, so the Alfvén radius is often referenced in the study of solar wind corotation and dynamics. Alfvén wave speed is derived from the magnetic-field intensity and plasma mass density. In the inner coronal regions, these parameters were previously estimated using empirical models based on remote sensing observations or from inverse-square scaling of measurements at 1 au. Parker Solar Probe (PSP) orbital encounters now provide in situ coronal plasma measurements to determine Alfvén speeds within 30 solar radii of the heliocenter. We combined the PSP solar-wind speed measurements and calculated Alfvén speeds with an inner corona wind speed profile from remote sensing studies. The zone of super-Alfvénic speed cross over is estimated to occur at mean heliocentric distance of $17.9 \pm 2.1 \, R_\odot$ for slow solar winds of the low heliolatitude corona in a near-minimum solar activity state. Our r_A values constrain the angular momentum flux to a mean of $3.5 \pm 1.01 \times 10^{22}$ N m sr^{-1}, reinforcing the recent PSP results by direct measurements of particle flows.

Unified Astronomy Thesaurus concepts: Solar wind (1534); Solar corona (1483)

1. Introduction

Solar wind (SW) acceleration is a complex phenomenon that occurs over an extended distance into the corona. MHD wave energy is believed to play an essential role in the process, transferring coronal magnetic energy to the developing solar wind. The balance between magnetic and kinetic energy in the SW is a key component controlling the dynamics and wind evolution. This balance changes with distance out into the corona and heliosphere. The main parameter for scaling MHD wave energy is the Alfvén speed, V_A:

$$V_A = \frac{B}{\sqrt{\mu_0 \rho}} \qquad (1)$$

with magnetic-field intensity B, permeability μ_0, and plasma mass density ρ (S.I. units). Energy density in a magnetic field, $\xi_B = \frac{B^2}{2\mu_0}$, may be rewritten in terms of Alfvén speed

$$\xi_B = \frac{1}{2}\rho V_A^2, \qquad (2)$$

which is then directly comparable to the solar wind kinetic energy density

$$\xi_{KE} = \frac{1}{2}\rho V_{SW}^2. \qquad (3)$$

If we consider the radial outflow speed, V_R, to be the main SW velocity component, then the Alfvénic mach ratio squared,

$$M_A^2 = (V_R/V_A)^2 \qquad (4)$$

indicates the balance between magnetic and kinetic energy in the SW for simplified, steady-state coronal conditions.

The energy balance is dominated by the kinetic energy when the SW outflow speed surpasses the Alfvén speed. The heliocentric distance to this speed cross over is called the Alfvén transition point, or Alfvén radius, r_A. In super-Alfvénic winds, both outwardly directed and retrograde Alfvén waves have net outward motion; there is no communication of MHD waves back to the inner corona. In contrast, below the Alfvén radius, the magnetic structuring of the corona is strong and retrograde MHD waves can still reach inner coronal regions to potentially enhance wave interactions and MHD energy transfer. An areal set of such points constitutes an Alfvén surface. Due to the considerable variability in bulk SW speeds and other plasma parameters, it is more realistic to describe a transition zone for the appearance of super-Alfvénic outflows (DeForest et al. 2018). Our main concern in this paper is to constrain the Alfvén radius and define the coronal zone of Alfvén speed transitions.

The Alfvén radius appears in the scaling of SW angular momentum flux (Weber & Davis 1967). Starting with Maxwell's equations applied to an equatorial plane steady-state corona with azimuthal symmetry, they integrated the azimuthal equation of motion to obtain the angular momentum carried away from the Sun per unit mass, L:

$$L = rV_\phi - \frac{B_R}{4\pi\rho\mu_0}rB_\phi \qquad (5)$$

where the first term on the right-hand side represents the contribution of particle azimuthal flows, and the second term represents the magnetic stresses. Further they showed that the magnetic field must arrange itself for varying speeds and M_A to produce a constant angular momentum per unit mass

$$L = \Omega r_A^2. \qquad (6)$$

We use $\Omega = 2.7 \times 10^{-6}$ rad/s as the effective solar rotation rate at low heliolatitudes.

The angular momentum multiplied by the mass flux yields the angular momentum flux in the system:

$$F(r) = \rho V_R r^2 \Omega r_A^2 \qquad (7)$$

in SI units N m sr^{-1}. Thus total angular momentum flux (the sum of particle and magnetic terms) can be obtained from knowledge of r_A and the solar-wind speed.

One approach to derivation of r_A has been the extrapolation of plasma parameters measured from a great distance. For example, Katsikas et al. (2010) and Goelzer et al. (2014) relied on extrapolation of wind and magnetic-field data from 1 au observations down to inner coronal regions by inverse-square scaling for electron number density, n_e, and magnetic-field strength, B, and simplifying assumptions for the estimation of V_{SW}. Another approach has been to use MHD heliospheric models to map the Alfvén surface, e.g., Chhiber et al. (2019). The modeled surface tends to be smooth, not directly incorporating the high variability of slow SW speeds and V_A fluctuations. However, global MHD models based on magnetogram-based boundary conditions may yield large-scale variations in the Alfvén radius, especially during solar maximum, as shown by Cohen (2015). It is desirable to obtain Alfvén radius estimates using source data closer to the speed transition region of concern. Inside the range of currently available PSP in situ observations, the Alfvén speed can be reasonably extrapolated inward roughly by $1/r$ scaling due the conservation laws for mass flux and magnetic flux, but the slow solar winds of the extended corona are variable and do not directly extrapolate inward to the acceleration region. Empirical models of coronal electron density for the SW acceleration zone can be used to scale the outflow speed, V_R, using mass–flux relation, $n_e V_R r^2 = Const$. This approach was taken by Wexler et al. (2020) to establish a slow SW acceleration profile based on analysis of transcoronal spacecraft radio frequency fluctuations. They utilized the Mercier–Hollweg electron density model

$$n_e = 6.5 \times 10^{13} r^{-5.94} + 7.7 \times 10^{11} (r-1)^{-2.25} \text{ [m}^{-3}\text{]} \quad (8)$$

in which V_R is essentially encoded by the power-law relation of the second term out to the intended outer limit of about $r = 20\,R_\odot$.

In the Parker Solar Probe (PSP) era, the spatial localization and dynamic implications of the Alfvén surface can be explored in greater detail than previously possible. Attempts to constrain the Alfvén distance by measuring the components of total angular momentum have been challenging. Réville et al. (2020) discussed the "angular momentum paradox" found with the early PSP data, for which the particle and magnetic contributions to total angular momentum implied an Alfvén radius too large to be consistent with the measured Alfvén Mach number. Liu et al. (2021), noting the uncertainties and potential problems with transverse velocity measurements, evaluated angular momentum flux and r_A using PSP observations of magnetic-field components and radial SW speed using a simplifying assumption for the presumed V_R at the Alfvén point but without reliance on azimuthal SW velocities. Finley et al. (2020) demonstrated the variability of total angular momentum using PSP particle and magnetic-field data primarily from the first two encounters.

The present work is a composite study bringing an SW speed profile implied by the above empirical electron density equation together with PSP in situ observations from five encounters. Until the PSP encounters yield velocity data at sufficiently low heliodistance, the use of established slow solar wind profiles can help constrain the Alfvén speed transition zone and calibrate the average angular momentum flux. This study is intended to produce estimates of SW total angular momentum and r_A, and characterize the range over which Alfvénic speed transitions are expected to be found.

This study focuses on the slow solar wind of low heliolatitudes during intervals of relatively steady behavior and well-defined power-law behavior of the pertinent plasma parameters in the PSP data over 2018–2020. The Sun was in a state of declining activity in cycle 24 into solar minimum leading to the onset of cycle 25. At solar minimum, the solar global magnetic structure corresponds to a near dipole configuration and the low-latitude corona has streamers and variable slow solar winds.

2. Methods

The general approach to finding the Alfvén radius directly involves establishing the intersection between the SW outflow speed, which we equate with the radial speed, V_R, and the Alfvén speed, determined computationally from the magnetic field and proton density PSP data. The magnetic-field data were measured by the FIELDS instrument suite (Bale et al. 2016) and the solar-wind-speed components and proton densities were measured by the SWEAP instrument package (Kasper et al. 2016).

We obtained publicly available PSP L3 SWEAP and L2 FIELDS data for encounters 1 (2018 November), 2 (2019 April), 4 (2020 January–February), 5 (2020 June), and 6 (2020 September–October) from the PSP Science Gateway.[3] The spacecraft reached heliocentric distances of 35.7 $R_\odot$ for perihelia 1 and 2, 27.8 $R_\odot$ during perihelion 4, 27.8 for perihelia 4 and 5, and 20.3 Rs for the subsequent perihelion 6. The scope of these data corresponded to the declining phase of solar cycle 24 into solar minimum and the beginning of solar cycle 25. As the PSP trajectories lie in near-equatorial heliolatitudes, the main winds encountered were expected to be of slow solar wind character. We restricted our study to the slow solar wind, <450 km s^{-1}.

The radial outbound solar-wind speed, V_R, and proton-number density, n_p, were obtained from the SWEAP data files. The absolute magnetic-field intensity, B_{TOT} was obtained from the combination in quadrature of the FIELDS components B_R, B_T, and B_N. Data quality flags set by the instrument teams were checked to exclude problematic data. Due to unavailable or unreliable data in the publicly released files, the analysis was limited to data beyond distance 27 $R_\odot$. The data were processed into consecutive 600 s averages.

The inbound trajectory encounters (Ei) were sufficiently different from the outbound trajectory encounters (Eo) to warrant separate analysis of individual semi-encounters. For this study we chose data segments that adhered generally to conventional power-law scaling on heliocentric distance, consistent with solar wind streams expanding freely into space. Other important structures such as current sheets and stream interaction regions might introduce punctuated disturbances to the power-law forms and degrade the analysis of the slow solar wind. Therefore, we applied a consistent approach to exclude the points that grossly deviated from the general power-law reference line.

Figure 1 shows inbound data for encounter 6 (E6i) and outbound data (E6o). As seen by comparison with the inverse-square reference line, parts of the data seemed suitable for the power-law fit and other parts were unsuitable. Among the latter were intervals of greatly diminished magnetic-field strength, as seen in Figure 1 (top panel, red) and increased proton density (top panel, black). The data were combined into a calculated
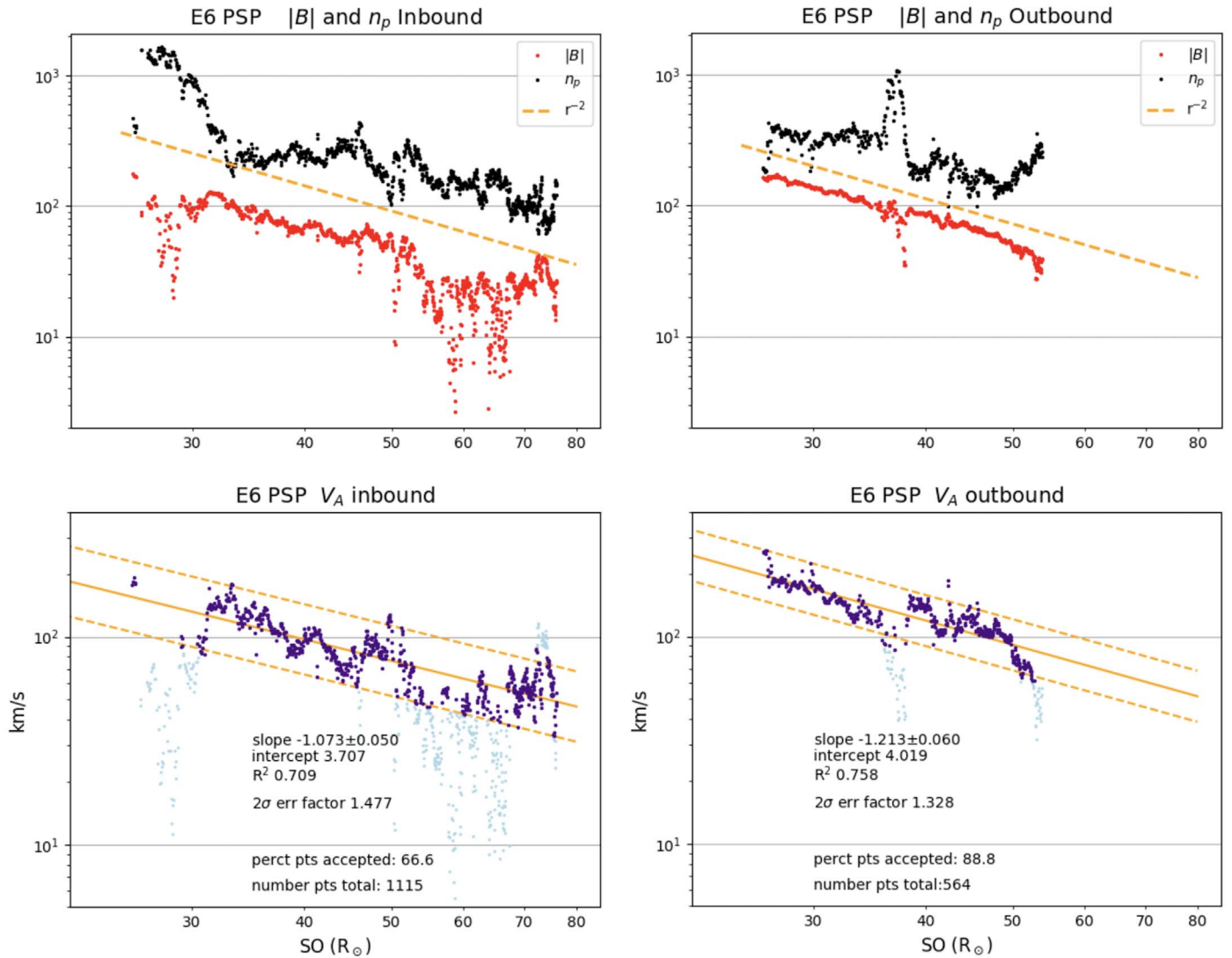
Figure 1. Determination of Alfvén speed power laws on heliocentric distance (solar offset, SO) for PSP encounter 6. The top panels show proton densities (cm^{-3}) and magnetic field strengths (nT) in comparison to an arbitrary inverse-square reference line. Clear departures from the inverse square are seen in limited segments, whereas most of the data generally follow the power-law scaling. The lower panels show the linear regression fit of calculated V_A points accepted (indigo) for the fitting procedure, and the excluded points (light blue).

V_A, and only points within 0.2 log of a coarse-fit inverse-square line for V_A were included for the fitting of the Alfvén speed. All other points were excluded; see the light blue data points in Figure 1, lower panel. The accepted V_A points were then fitted by linear regression in log–log format to find the coefficients α and γ in $V_A = 10^{\gamma} r^{\alpha}$. For each fit, the squared correlation coefficient, R^2, was considered a measure of goodness-of-fit. 2σ uncertainty bars were also determined for the log–log fits, corresponding to an uncertainly factor, W, of $10^{2\sigma}$. The uncertainties are assumed to be uncorrelated with one another, so the aggregate uncertainty is believed to reflect that of the observed parameters, not a systematic bias. The final fitted lines for V_A in the E6i and E6o samples are shown in Figure 1, lower panel. The V_A fitting and results are given in Table 1. For viewing purposes, the densities are shown in units of cm^{-3} and the magnetic field strengths in nT, but for calculated results, the S.I. conventions are used. Encounters E1o, E4o, and E5o were excluded from the final analysis. In the case of E1o, the wind speed over 40–50 $R_{\odot}$ was about 400–500 km s^{-1} and not representative of slow SW. The accompanying decrease in

electron density produced a disturbed VA profile over 40–50 $R_{\odot}$, making the power-law fit of dubious value. With E4o and E5o, magnetic sector crossing was evident, with asymmetric polarity reversal and relatively sparse magnetic-field data suitable for the power-law scaling below 40 Rs. The E4o and E5o semi-encounters excluded in this study may be of interest for a separate analysis of magnetic sector crossings.

In the PSP data sets, V_R was always greater than the calculated V_A down to the inner radial limit of usable data, so determination of the Alfvén radius required estimating the SW speed profile down into the region $<27\,R_{\odot}$. For this purpose, a slow solar wind model as presented in Wexler et al. (2020) was applied (Figure 2). This SW model was developed from analysis of transcoronal spacecraft radio frequency fluctuations, described as

$$V_{\mathrm{SW}} = S\frac{1.11 \times 10^{17}}{n_e r^2}\ [\mathrm{m/s}] \qquad (9)$$

where the electron number density, n_e, is given by Equation (8) and S is the scaling factor applied to match the inner coronal V_R

Table 1
Power-law Fitting for V_A and Wind-speed Scaling

Encounter	S	α	γ	R^2	W
$E1_i$	0.861	-0.938 ± 0.085	3.424	0.363	1.417
$E2_i$	0.851	-1.062 ± 0.037	3.751	0.674	1.604
$E2_o$	0.974	-1.335 ± 0.059	4.165	0.724	1.539
$E4_i$	0.968	-0.896 ± 0.037	3.522	0.634	1.531
$E5_i$	0.832	-0.960 ± 0.031	3.436	0.717	1.541
$E6_i$	0.834	-1.073 ± 0.050	3.707	0.709	1.477
$E6_o$	1.014	-1.231 ± 0.060	4.019	0.758	1.328
Average	0.905 ± 0.077	-1.068 ± 0.158	3.717 ± 0.289	0.654	1.491

Note. Scaling factor, S, applied to the V_{SW} model; α and γ are the power-law components from the linear regression. The density is given as cm^{-3}; R^2 is the Pearson coefficient squared; W is the 2σ uncertainty in the log–log regression line.
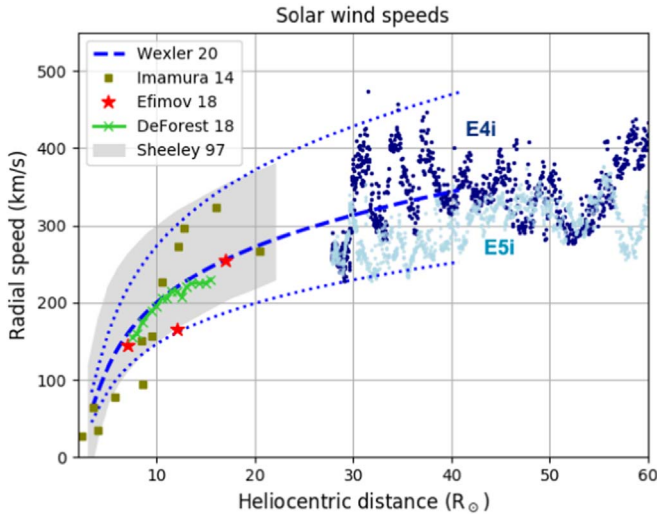

Figure 2. Composite solar-wind-speed profile. In situ measurements from PSP start at $28\,R_\odot$, with E4i and E5i samples given. A summary of SW speeds from remote sensing (see Wexler et al. 2020) is shown up to $22\,R_\odot$. Equation (9) for V_{SW} (blue dashed line), with uncertainty limits (blue dotted lines), is extrapolated to $40\,R_\odot$ in order to demonstrate the overlap with the PSP wind-speed measurements. Here the scale factor S is unity.

estimate with in situ measurements of SW speed recorded by the PSP.

The SW speed model was developed to describe the SW speed profile for radial heliocentric distance (the solar offset, SO) range 2–$20\,R_\odot$, but is here extrapolated out to $40\,R_\odot$ to verify the overlap with PSP radial speed data (Figure 2). The error limits in the SW speed model are a factor of 1.367 as developed in the original work. Also shown for comparison are the white light speed data from Sheeley et al. (1997) and DeForest et al. (2018), as well as the radio scintillation results from Imamura et al. (2014) and the two-station radio studies by Efimov et al. (2018). Collectively, these show a broad but consistent range of values for slow SW acceleration.

In Figure 2 the PSP in situ V_R speed results are noted to overlap into the SW range extrapolated from the radio data fairly well even with the scale factor S set to unity. However, the two-sample SW PSP profiles meet the radio SW speed curve at different levels. Accordingly, for purposes of this study, the wind speed Equation (9) was scaled linearly by a factor S, to match the PSP V_R data up to $r = 40\,R_\odot$ by least squares fit. A best-fit scaling coefficient was obtained for each of the seven semi-trajectories used in this study (Table 1). The

mean SW scaling coefficient S was 0.905 and the range was 0.832–1.104. These scalings suggest that the number density model used and assumption of mass flux scaling for SW speed were suitable for the PSP data of these encounters.

For each PSP encounter, r_A was determined as the intersection of V_A and the scaled solar-wind-speed model. The range for each r_A was determined from the intersection of the uncertainty limits for both V_A and V_R. The associated total angular momentum flux F was calculated using Equation (7), with V_R from Equation (9) and the number density from Equation (8) using $r = r_A$.

3. Results

The Alfvén radius and total angular momentum flux for all encounters studied are summarized in Table 2. The mean r_A was $17.9 \pm 2.1\,R_\odot$. For individual encounters, the r_A range was as low as $9.1\,R_\odot$ and as high as $30.0\,R_\odot$. The mean angular momentum flux was $3.50 \pm 1.01 \times 10^{22}\,\mathrm{N\,m\,sr^{-1}}$.

Four samples of individual encounter results are given in Figure 3. SW speed is clearly higher than Alfvén speed beyond $35\,R_\odot$, with Alfvén mach numbers always above one, and gradually increasing. Based on the variability in the data, convergence of the V_{SW} curve and V_A curves produced a broad range of intersection, representing the zone of SW Alfvénic speed transition as 9–$30\,R_\odot$.

There is good agreement between the generalized SW speed radial profile from remote sensing and projected beyond $30\,R_\odot$ and the observed speeds from PSP. In these data, the SW speed reaches a plateau by about $40\,R_\odot$. The known high variability in SW speeds is well demonstrated by the PSP measurements and is similar to that seen in remote sensing studies.

Also shown in Figure 3 are subpanels for the plasma β (ratio of thermal pressure to magnetic pressure), the Alfvénic Mach ratio and the fraction of solar wind KE, ϵ_{KE} (fraction of KE to sum of KE, magnetic energy, and thermal energy as obtained from PSP data). Of note in these findings, M_A was sometimes close to one but always greater than unity down to our inner limit of $28\,R_\odot$. Both M_A and ϵ_{KE} generally increased with increasing heliocentric distance. Plasma β was variable. SW KE dominated the SW energy regardless of whether plasma β was greater or less than one. Thus, beyond the Alfvén radius, the plasma thermal energy is far exceeded by the local KE even in the low β condition. In general, increased β was associated with increased M_A and diminished V_A.

At a given heliodistance, solar-wind-outflow speed and Alfvén speed are numerically linked through the density parameter in the mass–flux relation, so V_A/B is expected to

<div align="center">

Table 2
Summary of Results

</div>

Encounter	r_A	Range	Model at r_A		PSP at 40 $R_\odot$			
			V_R	F_{r_A}	V_R	V_A	M_A	$|B|$
E1$_i$	15.1	9.5–24.8	210	2.31	278	82	3.4	70.4
E2$_i$	18.6	11.7–30.0	225	3.46	279	86	3.2	71.8
E2$_o$	20.3	13.2–30.0	266	4.72	327	137	2.4	79.2
E4$_i$	17.9	10.4–30.0	252	3.64	345	127	2.7	71.3
E5$_i$	15.1	9.1–26.3	203	2.23	290	90	3.2	63.1
E6$_i$	18.6	11.7–30.0	221	3.39	303	95	3.2	69.0
E6$_o$	20.0	13.9–29.3	276	4.77	324	131	2.5	84.7
Average	17.9 ± 2.1		236 ± 28	3.50 ± 1.01	306 ± 26	107 ± 24	2.9 ± 0.4	72.8 ± 7.1

Note. Alfvén radius r_A (in $R_\odot$), r_A range ($R_\odot$) resulting from the variability in V_A and V_R, total angular momentum flux ($\times 10^{22}$, in N m sr^{-1}), values at 40 $R_\odot$ (as averages over 38.8–41.5 $R_\odot$) for PSP radial speed V_R (km s^{-1}), calculated V_A (km s^{-1}), Alfvénic Mach number, M_A, and magnitude of magnetic field strength, B (nT).

scale in proportion to $\sqrt{V_R}$. We found that these quantities, as individual encounter averages at 40 $R_\odot$ given in Table 2, have a Spearman correlation coefficient of $R = 0.964$ ($p < 0.001$). This serves as an additional check that mass–flux power-law scaling is upheld in the included data segments. Also, we found a correlation between V_A and r_A, $R = 0.764$ ($p < 0.05$), and between B and r_A, $R = 0.782$ ($p < 0.05$).

4. Discussion

For low-latitude regions, the mean Alfvén radius was found to be $17.9 \pm 2.1\ R_\odot$. These results are applicable to slow-wind regions for which the power-law scaling in magnetic-field intensity and proton-number density are generally upheld. Our mean Alfvén radius value is consistent with the conclusion of DeForest et al. (2014) that r_A for streamer-belt regions should be found beyond 15 $R_\odot$. The mean V_A power-law index of -1.068 ± 0.158 shows that the overall inverse-square scaling was representative in the n_e and B data included in the analysis. There were other PSP data segments, not included here, which showed significant departures from the conventional scaling that may indicate the presence of structures, currents, and transient phenomena. Evaluation of these segments will require different analytical approaches.

The full possible extent of the Alfvén speed transition zone in this study ranged as low as 9.1 $R_\odot$ and as high as 30 $R_\odot$ for the near-equatorial corona. This range is broader than that from simulations by Chhiber et al. (2019), which illustrated an Alfvén transition region ranging over 10–19 $R_\odot$ for low heliolatitudes at low-to-medium solar activity. Verscharen et al. (2021), using 30 hr averages of Ulysses data, demonstrated the latitudinal and solar-cycle variation of r_A. High variability in low-latitude r_A was noted, ranging 0.1–28 $R_\odot$ during solar minimum. The simulations of Cranmer et al. (2007) contained Alfvén surfaces between 7 and 15 $R_\odot$ for solar minimum. Our range is wider due to the variability in both SW speeds (Figure 2) and V_A (Figure 1). In the case of the PSP wind speed data, the high variability does not necessarily mean a given stream is highly unstable; the variations are in part due to PSP probing different streams along its trajectory. A great range of Alfvén speeds in the inner corona was also reported by Evans et al. (2008) using coronal MHD models. Our results support the concept of a transition zone to super-Alfvénic outflow speeds (DeForest et al. 2018) rather than a simple Alfvén radius or smooth surface. In this zone of mixed sub-Alfvénic and super-Alfvénic winds, there is high likelihood of increased shear flows and MHD wave interactions (Ruffolo et al. 2020) and increased

turbulence (Matthaeus et al. 1999). With the coming PSP solar encounters, the Alfvén zone should be penetrated to allow direct observations of these MHD wave phenomena.

In contrast to the broad zone of Alfvén speed transitions mentioned above, the mean r_A is intended to scale the overall SW angular momentum. We obtained this value without use of particle transverse velocities. Attempts to calculate angular momentum from direct plasma magnetic field and velocity components have been complicated by technical uncertainties, particularly in the transverse velocity observations (e.g., Finley et al. 2020; Liu et al. 2021; Verscharen et al. 2021). From that point of view, our finding of $F = 3.50 \pm 1.01 \times 10^{22}$ N m sr^{-1} provides important confirmation of the ranges of globally averaged values determined by Finley et al. (2020), 2.6–4.2 $\times$ 10^{22} N m sr^{-1}. Further, our results reintroduce the "angular momentum paradox" (Réville et al. 2020). Using the mean values in Equation (14) from Weber & Davis (1967)

$$v_\phi(r) = \frac{\Omega r}{V_R(r_A)} \frac{V_R(r_A) - V_R(r)}{1 - M_A^2} \qquad (10)$$

we find an expected tangential proton speed of 3 km s^{-1} at distance 40 $R_\odot$ using the average values from Table 2. This is much below the average observed tangential speeds obtained by the SPC instrument on the PSP SWEAP assembly. Resolution of the discrepancy has been approached by considering pressure anisotropy (Réville et al. 2020) and the contributions of alpha particles to the total angular momentum (Li et al. 2007; Liu et al. 2021) and global averaging of widely varying particle fluxes (Finley et al. 2020). The role of alpha particles, with an average relative abundance of 5% corresponding to about 20% of the mass density, was not considered here but does warrant further attention in the study of SW angular momentum. As work continues to remove the remaining uncertainties in the measurement of tangential fluxes, our estimates of r_A and angular momentum flux, obtained from multiple PSP encounters without the use of tangential speed measurements should be useful.

Liu et al. (2021) recently reported a mean Alfvén radius of 9.7 $R_\odot$, with range 8.1–11.8 $R_\odot$, using magnetic field and velocity data from the first four PSP encounters. Their values lie in the lower end of the range we report here. The individual encounter values were lower by a factor of nearly 2 compared to the results given in this paper. The discrepancy may arise from their assumption that the SW speed did not increase significantly beyond the Alfvén point, yielding the approximation $r_A \sim r/M_A$.
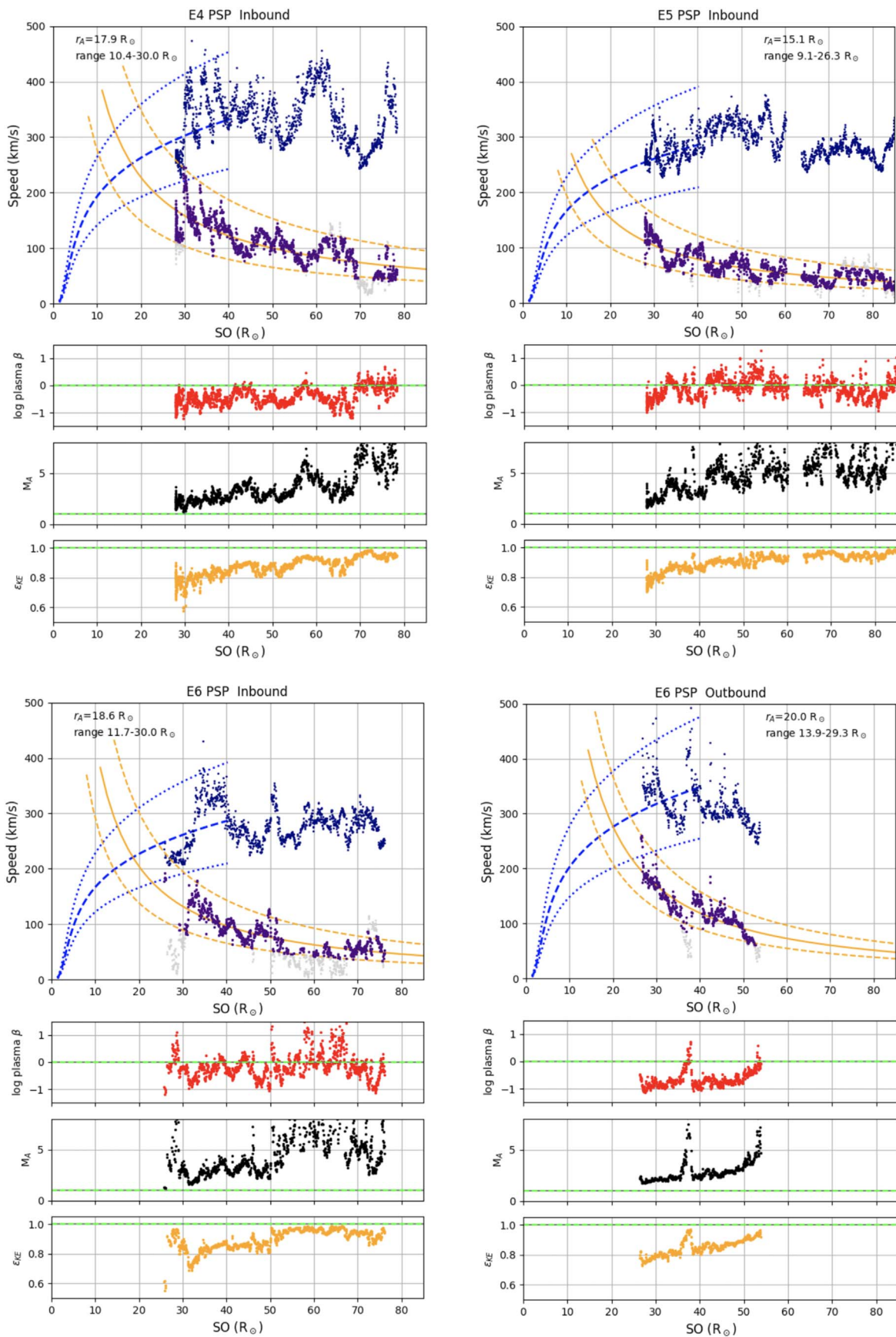
Figure 3. Comparison of radial solar-wind speeds and Alfvén speeds. In situ measurements from PSP start at 28 $R_\odot$ with V_R in deep blue and V_A in indigo; the fitted Alfvén speed curve (orange solid line) is extended to the inner corona, with 2σ variability limits (dashed orange lines). SW speeds from Equation (9) are shown up to $r = 40\ R_\odot$ (blue dashed lines), with error limits (dotted blue lines). For each encounter, the corresponding curves for plasma β, M_A and the fractional kinetic energy ϵ_{KE} are also given.

However, at the mean radius of $9.7\,R_\odot$, there is typically still considerable SW acceleration to occur over the next 10–$20\,R_\odot$ (see Figure 1). According to the foundational work by Weber & Davis (1967), if the speed at the Alfvén point is the same as in the extended corona, the particle transverse velocity contribution to the angular momentum flux is zero, making the momentum entirely based on the magnetic field components. Thus, the mean angular momentum flux of $1.5 \times 10^{22}\,\mathrm{N\,m\,sr^{-1}}$ in Liu et al. (2021) is probably low, reflecting mostly the magnetic stress contribution.

The Alfvén radius varies with solar cycle. Using WIND spacecraft observations at L1, Kasper & Klein (2019) estimated an average Alfvén radius of $20\,R_\odot$ (range of about 15–$25\,R_\odot$) during the relative quiescence of solar cycle 23. Our results also generally agree with those reported by Goelzer et al. (2014) and Katsikas et al. (2010). Goelzer et al. (2014) studied the dependence of the Alfvén radius on the state of solar activity. Using sunspot counts with the associated plasma density and magnetic field measurements at one au from Omni2 observations over 1975–2013, they demonstrated a clear relation between the phase of the solar cycle and the Alfvén distance. Using their descriptive model for low solar activity conditions (e.g., sunspot count 3) with our data, we calculate an estimated $r_A = 15.5\,R_\odot$. Katsikas et al. (2010) evaluated the Alfvén transition surface using observations from the Ulysses spacecraft in 26 day averages. The Alfvén radius was found to extend out more broadly into the corona during increased solar activity. They found $\langle r_A \rangle = 19\,R_\odot$, with range 10–$30\,R_\odot$ overall and a contracted range of 12–$18\,R_\odot$ during solar minimum. All of these studies are subject to limitations of extrapolating back from averaged observations at 1 au. Our study, while also including averaged data for the wind speeds, was based on observations taken much closer to where the Alfvén transition zone would be expected.

Although the SW in streamer regions may become super-Alfvénic well within $30\,R_\odot$, the striated formations observed in white light often continue outward beyond this region. DeForest et al. (2016) describe the transformation from streamer striae to broad "flocculae" occurring beyond about $40\,R_\odot$ as the winds become more isotropic in large-scale ordering. Ruffolo et al. (2020) noted that the "slippage" of tangential wind flows from a magnetically controlled corotation state was consistent with the spacecraft being beyond the critical Alfvén speed transition zone. The partial persistence of magnetically controlled coronal structure and flow features into the super-Alfvénic regions may be related to the variable crossing of the $\beta = 1$ threshold (see Figure 3 subpanel, Chhiber et al. 2019, 2018, and DeForest et al. 2016). The coming PSP perihelion encounters, which will reach down to just inside $10\,R_\odot$, are expected to demonstrate decreasing SW speed and increasing Alfvén speed, with intermittent penetration of the Alfvén radius and enhanced magnetic structuring of the plasma flow.

ORCID iDs

David B. Wexler ● https://orcid.org/0000-0002-5763-6267
Michael L. Stevens ● https://orcid.org/0000-0002-7728-0085
Anthony W. Case ● https://orcid.org/0000-0002-3520-4041
Paul Song ● https://orcid.org/0000-0001-5938-8108

References

Bale, S. D., Goetz, K., Harvey, P. R., et al. 2016, SSRv, 204, 49
Chhiber, R., Usmanov, A. V., DeForest, C. E., et al. 2018, ApJL, 856, L39
Chhiber, R., Usmanov, A. V., Matthaeus, W. H., & Goldstein, M. L. 2019, ApJS, 241, 11
Cohen, O. 2015, SoPh, 290, 2245
Cranmer, S. R., van Ballegooijen, A. A., & Edgar, R. J. 2007, ApJS, 171, 520
DeForest, C. E., Howard, R. A., Velli, M., Viall, N., & Vourlidas, A. 2018, ApJ, 862, 18
DeForest, C. E., Howard, T. A., & McComas, D. J. 2014, ApJ, 787, 124
DeForest, C. E., Matthaeus, W. H., Viall, N. M., & Cranmer, S. R. 2016, ApJ, 828, 66
Efimov, A. I., Lukanina, L. A., Chashei, I. V., et al. 2018, CosRe, 56, 405
Evans, R. M., Opher, M., Manchester, W. B., IV, & Gombosi, T. I. 2008, ApJ, 687, 1355
Finley, A. J., Matt, S. P., Réville, V., et al. 2020, ApJL, 902, L4
Goelzer, M. L., Schwadron, N. A., & Smith, C. W. 2014, JGRA, 119, 115
Imamura, T., Tokumaru, M., Isobe, H., et al. 2014, ApJ, 788, 117
Kasper, J. C., Abiad, R., Austin, G., et al. 2016, SSRv, 204, 131
Kasper, J. C., & Klein, K. G. 2019, ApJL, 877, L35
Katsikas, V., Exarhos, G., & Moussas, X. 2010, AdSpR, 46, 382
Li, B., Habbal, S. R., & Li, X. 2007, ApJ, 661, 593
Liu, Y. D., Chen, C., Stevens, M. L., & Liu, M. 2021, ApJL, 908, L41
Matthaeus, W. H., Zank, G. P., Oughton, S., Mullan, D. J., & Dmitruk, P. 1999, ApJL, 523, L93
Réville, V., Velli, M., Panasenco, O., et al. 2020, ApJS, 246, 24
Ruffolo, D., Matthaeus, W. H., Chhiber, R., et al. 2020, ApJ, 902, 94
Sheeley, N. R., Wang, Y.-M., Hawley, S. H., et al. 1997, Astrophys J., 484, 472
Verscharen, D., Bale, S. D., & Velli, M. 2021, MNRAS, 506, 4993
Weber, E. J., & Davis, L. J. 1967, ApJ, 148, 217
Wexler, D., Imamura, T., Efimov, A., et al. 2020, SoPh, 295, 111